Emergent solution based IGZO memristor towards neuromorphic applications

Raquel Azevedo Martins, Emanuel Carlos, Jonas Deuermeier, Maria Elias Pereira, Rodrigo Martins, Elvira Fortunato, and Asal Kiazadeh**

CENIMAT/i3N Departamento de Ciência dos Materiais, Faculdade de Ciências e Tecnologia (FCT), Universidade NOVA de Lisboa (UNL), and CEMOP/UNINOVA, 2829-516 Caparica, Portugal. *E-mail: a.kiazadeh@fct.unl.pt and e.carlos@campus.fct.unl.pt (corresponding authors)

Abstract

Solution-based memristors are emergent devices, due to their potential in electrical performance for neuromorphic computing combined with simple and cheap fabrication processes. However, to reach a practical application in crossbar design it is required tens to hundreds of uniform memristors. Regarding this, the production steps optimization should be considered as main objective to achieve high performance devices. In this work, solution-based indium gallium zinc oxide (IGZO) memristor devices are produced using a combustion synthesis process. The device's performance is optimized by using different annealing temperatures and active layer thicknesses to reach a higher reproducibility and stability. All IGZO memristors show a low operating voltage, good endurance, and retention up to 10^5 s in air conditions. The optimized devices can be programmed in a multi-level cell operation mode, with 8 different resistive states. Also, preliminary results reveal synaptic behavior by replicating the plasticity of a synaptic junction through potentiation and depression, this being a significant step towards low-cost processes and large-scale compatibility of neuromorphic computing systems.

Keywords: IGZO, memristor, solution-based metal oxides, artificial synapses, Internet of Things

1. Introduction

Over the years, there has been an increasing demand to build devices with higher speed, larger capacity for storage and lower power consumption due to the emergent requirements in Internet of Things (IoT) and artificial intelligence (AI) era. Non-volatile memories (NVM) are one of these ubiquitous devices and are typically known for their ability to store information for long periods of time (over 10 years) [1]. Currently, flash memories are the most common NVM, presenting a high endurance and speed performance [2 3]. However, this technology is reaching their physical limitations and it will be replaced by other opportune NVM in the future. Memristor is an emergent NVM that is highly promising and a viable alternative to flash [4 5]. These devices possess a faster operation, good endurance, multilevel cell operation and scalability [6]. Regarding electrical performance, memristor is based on a reversible resistive switching (RS) mechanism between a low resistance state (LRS) and a high resistance state (HRS). These state changes are due to redox reactions in valence change mechanism (VCM) memristors, that create and break conductive filaments (CF), when voltage stimuli is applied to the device. The CF is typically formed by the migration of oxygen anion species or by electromigration of metal cations in the active layer [7].

Neuromorphic computing has been a modern way to overcome the problems faced in Von Neumann´s architecture. This approach emulates the function of a human brain with extremely low power consumption [8]. In the biological process, synapses perform learning and memory functions by modulating the connection between neurons [9]. Thus, one of the main interests in memristors is for artificial neural networks (ANN), as a synaptic device [10 11]. The resistance of the memristor can operate as synaptic weight, which can be updated by changing the resistance states of the memristor device. However, in deep neural network (DNN) approach, the

memristors only require a linear and symmetric response on the plasticity characteristic, whereas in real synapses time and frequency must be considered [12].

In order to be compatible with roll-to-roll large-scale manufacturing and flexible production techniques [13], amorphous metal oxide semiconductor (AOS) materials came up as an alternative to conventional Si technology, especially amorphous indium gallium zinc oxide (IGZO) [14]. IGZO has been widely studied and applied in vacuum processed and solution-processed thin-film transistors (TFTs), due to its high transparency, carrier mobility, and environmental stability [15,16,17]. Building AOS-memristor devices by adopting techniques of mature flexible semiconductor electronic technology is vital for low-cost flexible ANN systems. Since both electronic devices (memristors and TFTs) can share the same material, processing steps and technology.

In this respect, IGZO exhibits RS characteristics, which is ideal for the active layer of a memristor, however there are few reports on solution processing memristor devices[18,19]. RS mechanism strongly depends on oxygen vacancies (V_o) present in IGZO, which through solution processes can be controlled by changing gallium concentration. A change in IGZO molar proportion, particularly an increase of gallium will suppress the generation of V_o, responsible for carrier transportation [18]. One promising method is solution combustion synthesis (SCS), used to convert precursor solutions into oxides with the addition of a fuel that leads to the initiation of a combustion reaction. The main advantage of this method is the reduction of the thermal budget required to initialize the precursors conversion [20]. This allows the fabrication of memristor devices via coating and printing techniques and the possibility of flexible substrates as long as a compatible annealing temperature is used [21,22,23]. It is noteworthy that these processes are scalable, much simpler and cheaper than the commonly used vacuum techniques. [24,25]

In general, solution-processed memristor devices are novel, and the technology is not yet as mature as the vacuum processed ones. High quality films are extremely dependent to the fabrication methods (furnace/oven, hotplate annealing, ultraviolet photochemical activation, and microwave irradiation) and conditions which are still under optimization [6]. Cho et al. showed that with microwave irradiation can reach high yield and uniformity IGZO memristors in a controlled environment (nitrogen) [26]. However, the main limitation of using this technique is the scale-up to roll-to-roll (R2R) compatible techniques of solution-based memristors. **Table 1** summarizes the state of the art of solution-based IGZO memristor devices.

In this work, we report on solution-based IGZO memristors and the study of the influence of the annealing temperature and active layer thickness on the device performance in air environment. The optimized IGZO (1:3:1) memristors show bipolar resistive switching behavior with low variability, good endurance, and retention time up to 10^5 s at air ambient, which surpasses the current state-of-the-art. These devices reveal a multilevel cell (MLC) characteristic, achieving 8 different resistive states, 3 bits per cell. Some preliminary results on the synaptic behavior of the solution-based IGZO memristors through potentiation and depression is also shown, proving that these devices are suitable for neuromorphic applications.

Table 1. Performance comparison of solution-based IGZO memristors.

Year	BE[a]/ TE[b]	T_{max} (°C)	$R_{ON/OFF}$/MLC	Retention (s)	Endurance (cycles)	Neuromorphic applications
2012 [18]	Al/Al	370	2.7/No	n.d.	10^2	No
2014 [27]	Pt/Ti	300	3×10^1/No	10^4	9×10^1	No
2014 [19]	Pt/Pt	130	>10/No	10^4	10^2	No
2017 [28]	Ti/Ti	350	>10/No	10^4	10^2	No
2018 [29]	ITO/Pt	150	Approx. 10^3/No	10^4	10^4	No
2020 [30]	Ni/Pt	250	Approx. 10^2/No	10^4	2.5×10^2	No
2021 [31]	Al/ITO	350	n.a./Yes	n.a.	n.a.	Yes
2021 [26]	Pt/Ti	MA[c]	10^1/Yes	10^4	10^3	Yes

This Work	Ti/Pt Ti/Au	200	10^2/Yes	10^5	10^2	No
		300	10^2/Yes	10^5	10^2	Yes

[a]Bottom electrode, [b]Top electrode, [c]Microwave Annealing, n.a. – not available

2. Experimental section

2.1. Precursor solution synthesis and characterization

Indium (III) nitrate hydrate ($In(NO_3)_3 \cdot xH_2O$, Sigma-Aldrich, 99.9 %), gallium (III) nitrate hydrate ($Ga(NO_3)_3 \cdot xH_2O$, Sigma-Aldrich, 99.9 %) and zinc nitrate hexahydrate ($Zn(NO_3)_2 \cdot 6H2O$, Sigma-Aldrich, 98 %) were separately dissolved in 2-methoxyethanol (2-ME, $C_3H_8O_2$, Fisher Chemical, 99 %) to produce metal precursor solutions with concentration of 0.2 M. The fuel (Urea, Sigma, 99 %) was added to each solution and maintained under constant stirring for 1h. In order to guarantee the redox stoichiometry of the reactions, the urea to indium nitrate, gallium nitrate and zinc nitrate molar proportion were (5/2):1, (5/2):1 and (5/3):1, respectively. IGZO precursor solution was prepared by combining the three precursor solutions made, to obtain a In_2O_3:Ga_2O_3:ZnO molar ratio of 1:3:1 with a 0.2 M concentration. The precursor solution was stirred for at least 36 h at room temperature and filtrated with PTFE filter (0.45 µm) before use.

Thermogravimetry and differential scanning calorimetry (TG-DSC) measurement (Netzsch, TG-DSC-STA 449 F3 Jupiter) was performed for the IGZO (1:3:1) solution under air atmosphere up to 550 ºC with a 10 ºC min^{-1} heating rate in an aluminum crucible.

2.2. Thin film deposition and device fabrication

MIM structures were fabricated on corning glass substrates (Soda-lime glass). Prior to deposition, all substrates were cleaned as mentioned in a previous report [22]. The bottom electrode, a Ti/Pt bilayer of 30 and 30 nm was first deposited on the substrate by e-beam evaporation (homemade apparatus). Then, the IGZO thin films were deposited by spin coating for 35s at 2000 rpm (Laurell Tecnhologies), forming a single layer. Each deposition was

followed by an immediate hotplate annealing at 200 ℃ or 300 ℃ for 30 min in air environment (relative humidity (RH): 43 – 63% at room temperature). This process was repeated several times (1, 3, 5 and 7 layers), with a 10 min UV/Ozone surface treatment between each deposition. After thin films fabrication, a multilayer of Ti/Au, 6 nm, and 60 nm, respectively, was deposited by e-beam evaporation as the top electrode (25 devices) using a physical mask for the electrodes (area of 1.96×10^{-3} cm^2) patterning.

2.3. Thin film and device characterization

Optical properties were obtained using a Perkin Elmer lambda 950 UV/VIS/NIR spectrophotometer by measuring transmittance (T) in the wavelength range of 250-2500 nm. The optical characterization can be found in the Supporting Information (Figure S1 in the ESI). Fourier transform infrared (FTIR) spectroscopy data of thin films deposited on Si substrates were recorded using attenuated total reflectance (ATR) sampling accessory (Smart iTR) equipped with a single bounce diamond crystal on a Thermo Nicolet 6700 Spectrometer. The spectra' were acquired as reported in Supporting Information (Figure S2 in the ESI). Atomic Force Microscopy (AFM, Asylum MFP3D) was performed to analyze the topology of the optimal IGZO sample (Figure S3 in ESI).

X-ray photoelectron spectroscopy (XPS) was measured with a Kratos Axis Supra spectrometer. A monochromatic Al K α source was used with an aperture of 110 μm and the analyzer was set to pass energy of 80 eV. For depth profiling, an argon cluster of 500 atoms was used, with a kinetic energy of 10 keV, and scanned over 1.5 mm^2. The data were analyzed with CasaXPS software.

Spectroscopic ellipsometry was used to measure the thin film thickness, with an energy range from 1.5 to 5.5 eV and an incident angle of 45° using Yvon Uvisel system. The acquired data

were modulated using the DELTAPSI software and the fitting procedure was done pursuing the minimization of error function (χ_2).

The quasi-static current-voltage (I-V) characteristics and the pulse studies of the devices were measured using Keithley 4200 SCS semiconductor analyzer connected to the Janis ST-500 probe station. The bias was applied to the top electrode maintaining the bottom electrode connected to ground. The speed of the measurements was at normal mode and the integration time was in auto setting.

3. Results and discussion

Figure 1 (a) illustrates a sample with the produced memristors on glass substrate. The bottom and top electrode are Ti/Pt and Ti/Au, respectively and IGZO is the active layer.

To highly improve the performance of the memristor, the right molar proportion and doping on the IGZO layer needs to be well defined [6]. To obtain high quality solution-based IGZO memristors, the study of gallium concentration is fundamental to improve the RS behavior since it suppresses the V_o generation, and therefore reduces the mobility [18].

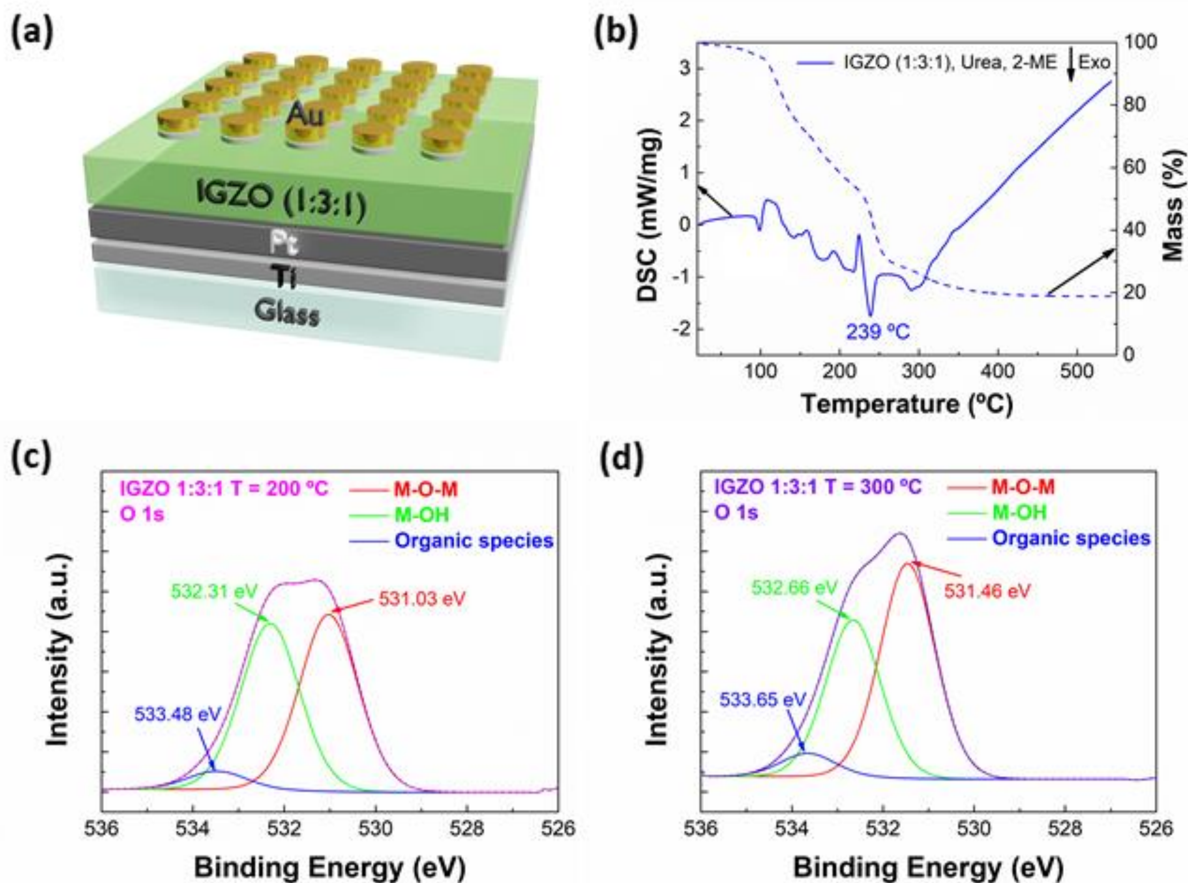

Figure 1. Schematic (a) of the IGZO (1:3:1) memristor device structure; (b) TG-DSC curves of IGZO (0.2 M) precursor solution with a molar ratio of 1:3:1; XPS surface spectra of samples annealed at: (c) 200 ºC and (d) 300 ºC.

TG-DSC was performed on the IGZO solution with a molar ratio of 1:3:1, as shown in **Figure 1** (b). The TG data points confirm that the precursor conversion is near complete under 250 ºC, with few reactions at higher temperatures related to some residual remaining organics. The DSC data points reveals one main exothermic peak during the combustion reaction at 239 ºC with a mass loss of approximately 34 %.

The optical transmittance of the IGZO thin films was measured to evaluate their transparency. The study shows a decrease from 90% to 87% of transmittance with the increment of deposited layers for all conditions, as depicted in Figure S1 in the ESI. The produced IGZO thin films were also characterized with ATR-FTIR in order to analyze the chemical bonds present, as

shown in Figure S2 in the ESI. AFM analysis (Figure S3 in ESI) shows that uniform and smooth surface was obtained. The IGZO thin films optimal condition present a surface roughness lower than 0.3 nm.

XPS analysis was performed in two samples annealed at different temperatures. **Figure 1** (c) and (d) present the XPS surface spectra' of a sample annealed at 200 ºC and 300 ºC, respectively. In both cases, O 1s is deconvoluted into three main peaks, each one corresponding to a different type of bond present in the sample. The first peak (red) is related to M-O-M bonds, the second (green) to M-OH bonds and the third peak (blue) is due to water and organic species adsorbed on the surface. These results reveal that at 300 ºC there is more presence of metal-oxygen bonds and less oxygen vacancies comparing with the peaks intensity at 200 ºC, which indicates that at higher temperature the devices are more resistive. The interface between the IGZO and the Pt bottom electrode was studied by argon cluster depth profiling, the respective spectra is presented in Figure S4 and S5 in the ESI. After most of the IGZO layer was removed, a significant C 1s emission could be detected in the sample annealed at 200 ºC (after 1100 s etch time), whereas the C 1s signal remained below the detection limit in the sample annealed at 300 ºC (after 1000 s etch time). This indicates that of organic compounds remain inside the film after an annealing at 200 ºC.

Spectroscopy ellipsometry was performed to measure the thickness of the active layers as depicted in Figure S6 in the ESI. An increase in deposited IGZO layers leads to an increment in thickness, regardless of the temperature used during the production of the memristors.

Concerning electrical performance, the pristine state of the IGZO memristors is considered the first I-V characteristic obtained. **Figure 2** (a) and (b) reveals the pristine state evolution when there is an increase of the active layer thickness. In both temperature conditions, the resistance increases with higher thickness. Also, devices annealed at 300 ºC show a similar tendency in

behavior, unlike devices annealed at 200 ºC, that have variable pristine curves. At 300 ºC the combustion reaction is completed and so, all the nitrate compounds are reduced to its metallic states. This can be explained since IGZO combustion reaction occurs until 250 ºC as observed in **Figure 1** (b), meaning that the use of lower annealing temperatures leaves residues of organic compounds, harming their performance. This is corroborated by the XPS analysis, which indicates that devices annealed at 200 ºC have more M-OH groups and organic compounds present, confirming that the combustion reaction was not completed.

The stoichiometry used promotes a high electrical resistivity of the devices since the gallium oxide present in IGZO is an insulator material [27]. By increasing the thickness of the active layer in the memristor, the device gets more resistive and consequently it decreases its off-state current, as observed in the pristine curves (**Figure 2** (a) and (b)). The results achieved with devices under these conditions can be easily reproducible.

Further electrical tests were operated only on the samples with higher IGZO thickness since these ones showed a higher reproducibility. The conditions studied were memristors with higher IGZO thickness (i.e., number of deposited layers) annealed at 200 ºC or 300 ºC. To activate the RS, an electroforming step was performed, as shown in Figure S7 in the ESI. All the devices formed under a positive bias, between 1 V and 2.5 V. A current compliance (CC) had to be maintained to prevent the breakdown of the devices. The I-V curves exhibit bipolar resistive switching under a CC of 10 mA for one device produced at 200 ºC with lower IGZO thickness and 1 mA for the other conditions, as shown in **Figure 2** (c)-(f). The I-V characteristics were measured with a controlled voltage through the top electrode and under consecutive DC voltage sweeps.

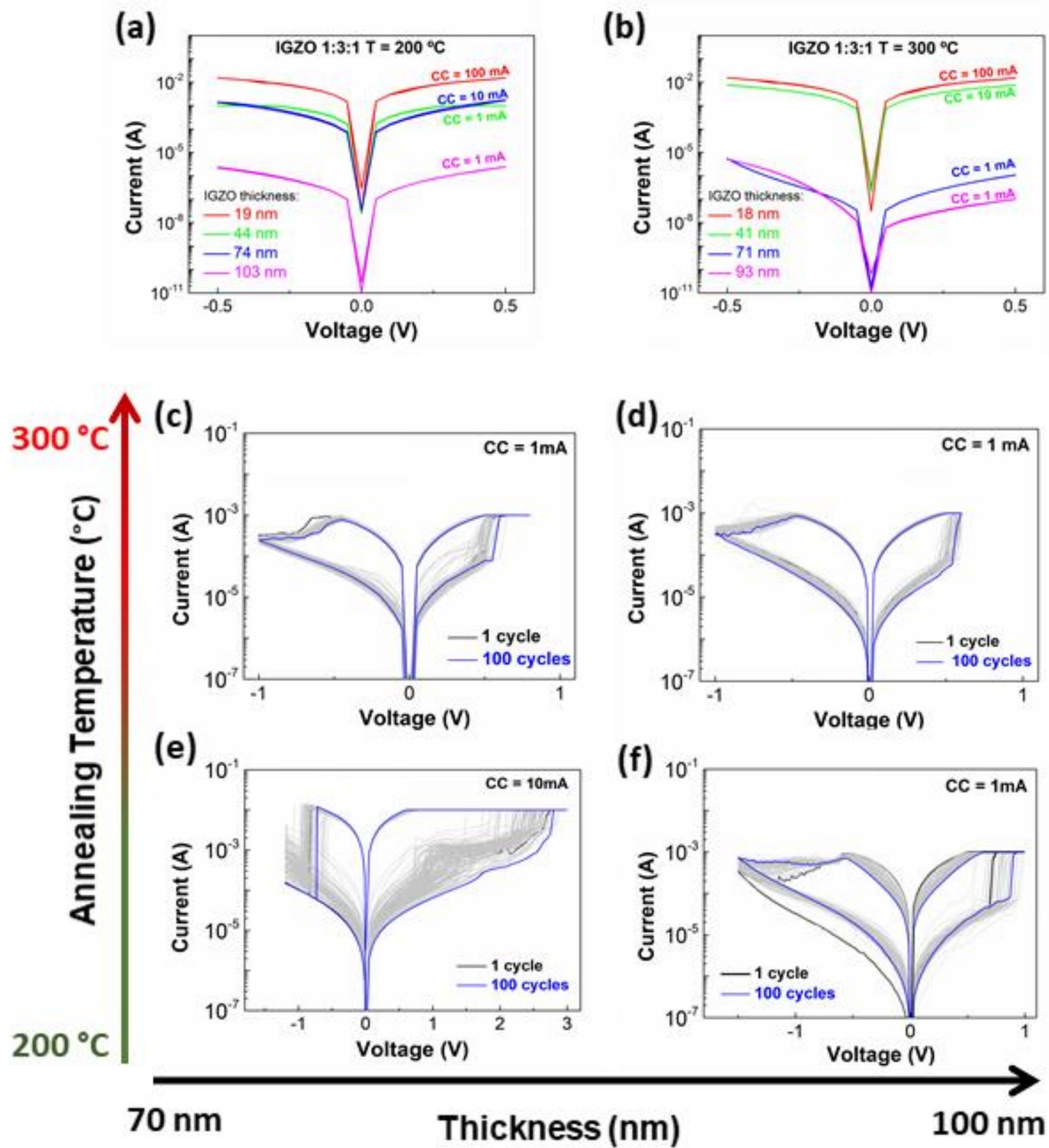

Figure 2. Ti/Pt/IGZO/Ti/Au electrical characterization. Pristine states of memristors with different IGZO thicknesses and annealed at (a) 200 ºC and (b) 300 ºC; *I*-*V* characteristics obtained from endurance tests during 100 cycles of memristors with different IGZO thicknesses: (c) and (d) devices annealed at 300 ºC; (e) and (f) devices annealed at 200 ºC.

The memristors reveal good endurance and a uniform switching behavior, although the devices annealed at 200 ºC present a higher variability (set and reset), as depicted in Figure S8 in the

ESI. The increase in temperature and active layer thickness reduces the deviation on set and the operating voltage. For a gradual reset there is no deviation in voltage, which is the case for devices annealed at 300 ºC and devices with a thicker active layer annealed at 200 ºC. In terms of conductance fluctuation, presented in Figure S9 in the ESI, both on and off states show higher variability in devices produced at 200 ºC. Memristors annealed at 300 ºC have smaller changes in both states. The annealing temperature has a higher influence on the conductance fluctuation than the thickness of the active layer. Thus, electrical results are in accordance with the material characterization studies (TG-DSC and XPS). The memristors annealed at 200 ºC have less metal-oxygen bonds in their structure, resulting in less stable devices. Whereas with an annealing of 300 ºC, the combustion reaction to form metal-oxygen bonds is completed. The produced devices have high stability and show great reproducibility being highly desirable for further upscaling techniques and applications.

Concerning the IGZO thickness, the thicker the layer the more stable the devices are, even the ones produced at lower temperature. This is due to the increased number of IGZO depositions that results in an increased number of annealing steps and fills the possible defects, improving the thin-film quality. Although a higher thickness reduces the probability of leakage, the annealing temperature is crucial to obtain a denser thin-film. Low annealing temperatures leave more organic residues than desirable, which interferes with the CF formation and consequently with the electrical performance.

Nevertheless, the condition that shows the best endurance and stability is the device depicted in **Figure 2** (d) annealed at higher temperature. Figure S10 in the ESI compares the set voltage of devices from two different batches that have the optimal thickness for a good electrical performance. Both batches present some variability due to the non-patterned devices structure.

Figure S11 in ESI represents a typical retention of the memristors in air ambient. This test reveals good retention of up to 10^5 s in air, with an $R_{ON/OFF}$ ratio of 10^2 and no significant degradation of HRS and LRS, meaning that these memristors are stable and non-volatile.

Another interesting feature of these memristors is the multilevel cell (MLC) behavior. The possibility of achieving more than two resistive states, allows the storage of more than 1 bit per cell which is highly important to achieve high densification [32]. **Figure 3** (a) shows the IV curves of the MLC characteristic obtained using the reset stop voltage method[33] to program different states. For each level programmed in the device a retention of 10^3 s was perform as depicted in Figure 3 (b). By using this methodology, it was possible to achieve 8 different resistance states (3 bits/cell) with a cycle-to cycle variation along for each state as shown in Figure 3 (c).

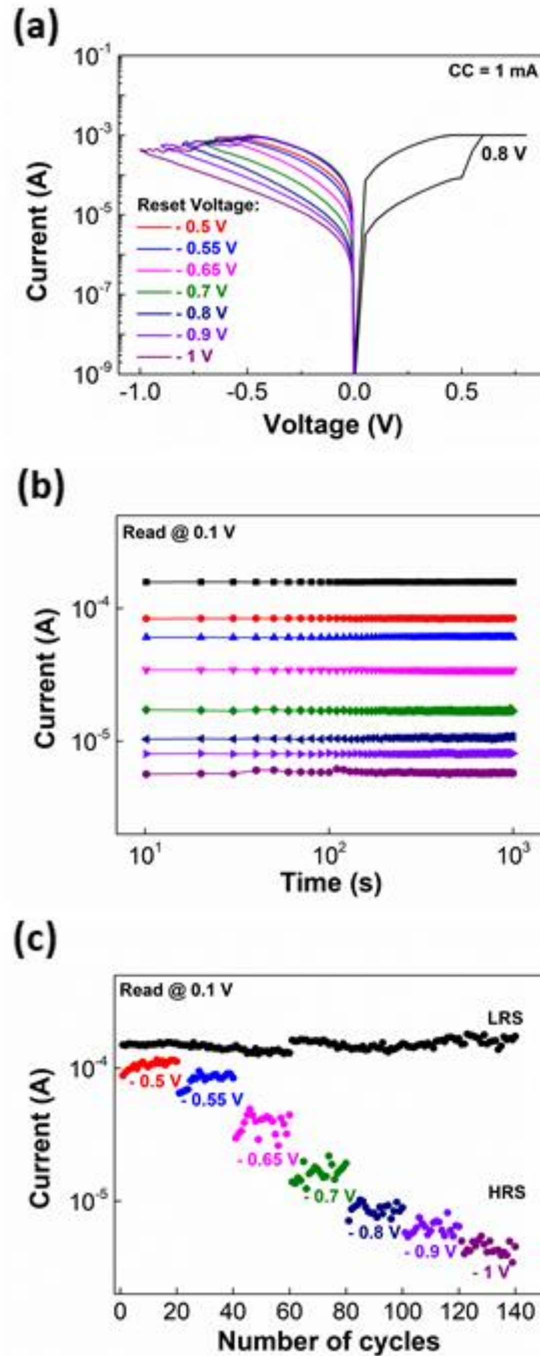

Figure 3. Solution-based IGZO (1:3:1) memristors: (a) Reset and set I-V curves of MLC retention; (b) MLC retention characteristics with read at 0.1 V during 10^3 s for seven different reset voltage; (c) Cycle to cycle MLC retention of the states presented in (b).

Since these devices are capable of MLC storage, a feature required for neuromorphic applications [34], pulse measurements were performed only on the best device conditions mentioned previously.

The accumulative behavior of the memristor is a key performance for in-memory computation and realized as the weight update in the training process of a neural network hardware. Preliminary results show that device can replicate the plasticity (potentiation/depression) of a synapse, when positive or negative consecutive pulses are applied[9]. Under a scheme of identical pulses, the current alteration can be translated to the change of synaptic weights. **Figure 4** (a) shows the typical conductance response to 100 positive consecutive pulses (potentiation) immediately followed by 100 negative pulses (depression), under a 0.1 V voltage read for 25 cycles. Regarding potentiation, pulses with 0.9 V of amplitude and 3.5 µs of width show a gradual exponential growth of conductance change with faster weight change at the beginning. Whereas, in depression, by applying pulses with -1.2 V of amplitude and 10 µs width is observed a gradual exponential reduction of conductance.

Generally, depression conductance variations to fully reset state can be better gradually controlled (Also as shown in Figure S12 in the ESI).

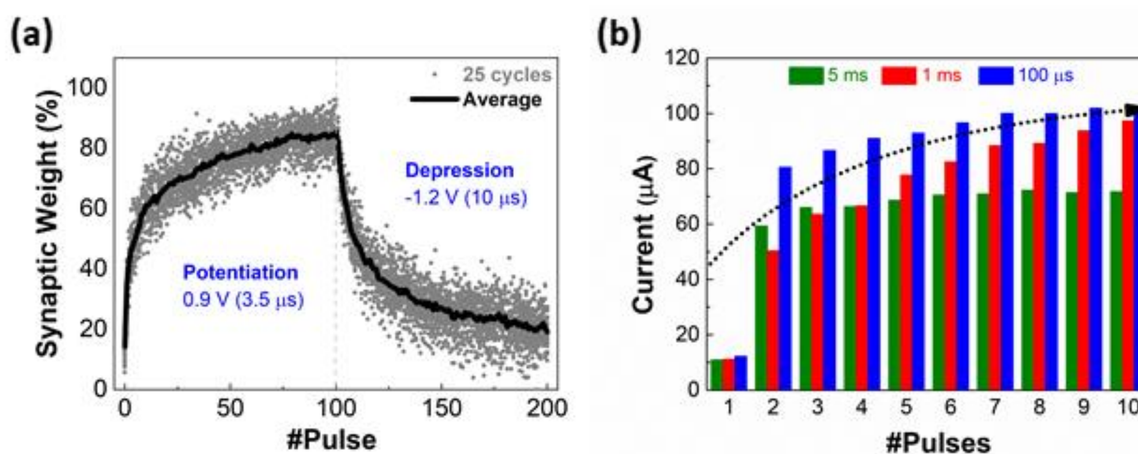

Figure 4. Solution-based IGZO device: (a) Synaptic weight change in percentage of 25 cycles for 100 consecutive pulses (potentiation and depression) under 0.1 V voltage read.; (b) Mean

change of ΔI of current during cycles of 10 pulses with different intervals: 5 ms, 1 ms and 100 μs.

Spike rate dependent plasticity as shown in **Figure 4** (b) is one of the basic characteristics to demonstrate the effect of pulse rates on synaptic weight of the device. It is one of the requirements of spiking neural network (SNN) systems where it incorporates the concept of time into operation similar to what happens in biology. Nevertheless, coding methods and efficient learning algorithms of SNN are not widely explored yet, hence exist many challenges for full adoption of memristor technology. On the other hand, memristors can be programmed into various resistance states by applying different pulses and are capable of in-memory computation by accumulative behavior (progressively reducing/increasing resistance) which is fundamental in training artificial neural networks (ANNs). However, symmetric and linearity of memristor responses greatly impact on the network accuracy.[35]

As final note, towards successful design of the all-solution processed neuromorphic system, the current IGZO memristor is required to be integrated with thin film transistors as reported by our group.[24] Such configuration of 1T1R allows an easy and efficient programming of devices into linear and symmetric synaptic responses by modulation of the transistor channel resistance via gate voltage bias.

4. Conclusions

Solution-based memristors have a lot of potential due to their scalable production at low cost, with more environmentally friendly techniques. Yet, there are some challenges to overcome in production, such as low uniformity over large area, something that directly affects the devices electrical performance in terms of reproducibility, stability, and variability. In this work, we surpass some of these issues by producing IGZO memristors using several layer depositions to minimize the stability problems. Also, the selection of proper IGZO molar proportion (1:3:1) was important for improved RS characteristics. The right production methods and an adequate active layer thickness, show an increased stability and device-to-device reproducibility. The MLC characteristics and synaptic behavior presented, revealed promising results for neuromorphic computing for future large-scale manufacturing with diverse IoT applications.

ASSOCIATED CONTENT

Electronic Supplementary Information (ESI)

The supplementary information contains relevant data related to the material and electrical characterization of the memristors. Figure S1 (a) and (b) shows the transmittance of IGZO thin films with several thicknesses, respected to each annealing temperature. Figure S2 (a) and (b) depict the FTIR spectra of IGZO thin films annealed with different temperatures. Figure S3 shows an AFM deflection image of an IGZO sample. Figure S4 and Figure S5 contains the XPS depth profiles performed in samples annealed at 200 ºC and 300 ºC, respectively. Figure S6 depicts the ellipsometry spectroscopy values of thickness of the active layer correspondent to the number of IGZO layers deposited. Figure S7 shows the electroforming of the IGZO memristors. Figure S8 indicates the set and reset voltage variability of each device studied. Figure S9 contains the conductance fluctuation of on and off state of each studied memristor. Figure S10 presents a histogram of the set voltage distribution for two different batches. Figure S11 shows the typical retention time of the IGZO memristors. Figure S12 shows the response of depression with different pulse intervals.

AUTHOR INFORMATION

Corresponding Authors

*E-mail: e.carlos@campus.fct.unl.pt
*E-mail: a.kiazadeh@fct.unl.pt

Notes

The authors declare no competing financial interest.

Author Contributions

The sample fabrication and characterization were performed by R. A. Martins under the supervision by A. Kiazadeh and E. Carlos. The manuscript was prepared by R. A. Martins. All authors examined, commented, and have given approval to the final version of the manuscript.

ACKNOWLEDGEMENTS

This work is funded in part by National Funds through FCT - Fundação para a Ciência e Tecnologia, I.P., under the scope of the project UIDB/50025/2020. E. Carlos acknowledges the postdoctoral grant (Grant 951774) from the project FOXES. M.E. Pereira acknowledges the doctoral grant DFA/BD/8335/2020 from FCT. A. Kiazadeh acknowledges FCT/MCTES, project NeurOxide (PTDC/NAN-MAT/30812/2017). E. Fortunato acknowledges the ERC AdG grant 787410 from the project DIGISMART. We acknowledge to the project SYNERGY H2020-WIDESPREAD-2020-5, CSA, proposal nº 952169 and Emerging Printed Electronics Research Infrastructure, 2020-INFRAIA-2020-1, EMERGE, reference nº 101008701.

REFERENCES

1 F. Hui, E. Grustan-Gutierrez, S. Long, Q. Liu, A. K. Ott, A. C. Ferrari and M. Lanza, *Adv. Electron. Mater.*, 2017, **3**, 1600195.

2 M. Sako, Y. Watanabe, T. Nakajima, J. Sato, K. Muraoka, M. Fujiu, F. Kono, M. Nakagawa, M. Masuda, K. Kato, Y. Terada, Y. Shimizu, M. Honma, A. Imamoto, T. Araya, H. Konno, T. Okanaga, T. Fujimura, X. Wang, M. Muramoto, M. Kamoshida, M. Kohno, Y. Suzuki, T. Hashiguchi, T. Kobayashi, M. Yamaoka and R. Yamashita, *IEEE J. Solid-State Circuits*, 2016, **51**, 196–203.

3 Y. Kim, I. H. Park, S. Cho, J. G. Yun, J. H. Lee, D. H. Kim, G. S. Lee, S. H. Park, D. H. Lee, W. B. Sim, W. Kim, H. Shin, J. D. Lee and B. G. Park, *IEEE Trans. Nanotechnol.*, 2010, **9**, 70–77.

4 S. H. Jo, T. Chang, I. Ebong, B. B. Bhadviya, P. Mazumder and W. Lu, *Nano Lett.*, 2010, **10**, 1297–1301.

5 D. Ielmini, *Semicond. Sci. Technol.*, 2016, **31**, 063002.

6 E. Carlos, R. Branquinho, R. Martins, A. Kiazadeh and E. Fortunato, *Adv. Mater.*, 2020, **2004328**, 1–37.

7 *Advances in Non-Volatile Memory and Storage Technology*, Elsevier, 2019.

8 D. Kuzum, S. Yu and H.-S. P. Wong, *Nanotechnology*, 2013, **24**, 382001.

9 Y. Park and J.-S. Lee, *ACS Nano*, 2017, **11**, 8962–8969.

10 S. Choi, S. H. Tan, Z. Li, Y. Kim, C. Choi, P. Y. Chen, H. Yeon, S. Yu and J. Kim, *Nat. Mater. 2018 174*, 2018, **17**, 335–340.

11 G.-T. Go, Y. Lee, D.-G. Seo, M. Pei, W. Lee, H. Yang and T.-W. Lee, *Adv. Intell. Syst.*, 2020, **2**, 2000012.

12 X. Hong, D. J. Loy, P. A. Dananjaya, F. Tan, C. Ng and W. Lew, *J. Mater. Sci.*, 2018,

53, 8720–8746.

13 K. Ide, K. Nomura, H. Hosono and T. Kamiya, *Phys. status solidi*, 2019, **216**, 1800372.

14 X. Yu, T. J. Marks and A. Facchetti, *Nat. Mater.*, 2016, **15**, 383–396.

15 P. G. Bahubalindruni, B. Silva, V. G. Tavares, P. Barquinha, N. Cardoso, P. Guedes De Oliveira, R. Martins and E. Fortunato, *IEEE/OSA J. Disp. Technol.*, 2015, **11**, 547–553.

16 C. Duarte, E. Fortunato, P. Barquinha, P. G. de Oliveira, P. G. Bahubalindruni, R. Martins and V. G. Tavares, *J. Disp. Technol. Vol. 9, Issue 12, pp. 1001-1006*, 2013, **9**, 1001–1006.

17 M. Moreira, E. Carlos, C. Dias, J. Deuermeier, M. Pereira, P. Barquinha, R. Branquinho, R. Martins and E. Fortunato, *Nanomaterials*, 2019, **9**, 1273.

18 M.-S. Kim, Y. Hwan Hwang, S. Kim, Z. Guo, D.-I. Moon, J.-M. Choi, M.-L. Seol, B.-S. Bae and Y.-K. Choi, *Appl. Phys. Lett.*, 2012, **101**, 243503.

19 W. Hu, L. Zou, X. Chen, N. Qin, S. Li and D. Bao, *ACS Appl. Mater. Interfaces*, 2014, **6**, 5012–5017.

20 E. Carlos, R. Martins, E. Fortunato and R. Branquinho, *Chem. – A Eur. J.*, 2020, **26**, 9099–9125.

21 N. Gergel-Hackett, B. Hamadani, B. Dunlap, J. Suehle, C. Richter, C. Hacker and D. Gundlach, *IEEE Electron Device Lett.*, 2009, **30**, 706–708.

22 E. Carlos, R. Branquinho, A. Kiazadeh, J. Martins, P. Barquinha, R. Martins and E. Fortunato, *ACS Appl. Mater. Interfaces*, 2017, **9**, 40428–40437.

23 E. Carlos, A. Kiazadeh, J. Deuermeier, R. Branquinho, R. Martins and E. Fortunato, *Nanotechnology*, 2018, **29**, 345206.

24 M. Pereira, J. Deuermeier, R. Nogueira, P. A. Carvalho, R. Martins, E. Fortunato and A. Kiazadeh, *Adv. Electron. Mater.*, 2020, **6**, 2000242.

25 J. Deuermeier, A. Kiazadeh, A. Klein, R. Martins and E. Fortunato, *Nanomaterials*, 2019, **9**, 289.

26 S.-Y. Min and W.-J. Cho, *Nanomaterials*, 2021, **11**, 1081.

27 Y.-H. Hwang, I. Hwang and W.-J. Cho, *J. Nanosci. Nanotechnol.*, 2014, **14**, 8196–8200.

28 J. Rosa, A. Kiazadeh, L. Santos, J. Deuermeier, R. Martins, H. L. Gomes and E. Fortunato, *ACS Omega*, 2017, **2**, 8366–8372.

29 L. Li, Y. Chen, W. Qu, Y. He, H. Yang, N. Li, Y. Song and Y. Shen, *J. Sol-Gel Sci. Technol.*, 2018, **88**, 601–608.

30 D. Lee, M. C. Chun, H. Ko, B. S. Kang and J. Kim, *Nanotechnology*, 2020, **31**, 245202.

31 S. Song, M. Kim, G. Yoo, S. M. Kwon, J. S. Heo, S. K. Park and Y. H. Kim, *J. Alloys Compd.*, 2021, **857**, 158027.

32 S.-T. Kim and W.-J. Cho, *Semicond. Sci. Technol.*, 2018, **33**, 015009.

33 M. Ismail, H. Abbas, C. Choi and S. Kim, *J. Alloys Compd.*, 2020, **835**, 155256.

34 K. Moon, S. Lim, J. Park, C. Sung, S. Oh, J. Woo, J. Lee and H. Hwang, *Faraday Discuss.*, 2019, **213**, 421–451.

35 G. W. Burr, R. M. Shelby, A. Sebastian, S. Kim, S. Kim, S. Sidler, K. Virwani, M. Ishii, P. Narayanan, A. Fumarola, L. L. Sanches, I. Boybat, M. Le Gallo, K. Moon, J. Woo, H. Hwang and Y. Leblebici, *Adv. Phys. X*, 2017, **2**, 89–124.

Table of Contents (TOC)